PROJECTION-BASED REDUCED ORDER MODELING FOR SPACECRAFT THERMAL ANALYSIS

Jing Qian, Yi Wang*, Hongjun Song, Kapil Pant
CFD Research Corporation, Huntsville AL, 35806, USA

Hume Peabody, Jentung Ku, Charles D. Butler
Thermal Engineering Branch, NASA Goddard Space Flight Center, Greenbelt, MD, 20771, USA

ABSTRACT

This paper presents a mathematically rigorous, subspace projection-based reduced order modeling (ROM) methodology and an integrated framework to automatically generate reduced order models for spacecraft thermal analysis. Two key steps in the reduced order modeling procedure are described: (1) the acquisition of a full-scale spacecraft model in the ordinary differential equation (ODE) and differential algebraic equation (DAE) form to resolve its dynamic thermal behavior; and (2) the ROM to markedly reduce the dimension of the full-scale model. Specifically, proper orthogonal decomposition (POD) in conjunction with discrete empirical interpolation method (DEIM) and trajectory piece-wise linear (TPWL) methods are developed to address the strong nonlinear thermal effects due to coupled conductive and radiative heat transfer in the spacecraft environment. Case studies using NASA-relevant satellite models are undertaken to verify the capability and to assess the computational performance of the ROM technique in terms of speed-up and error relative to the full-scale model. ROM exhibits excellent agreement in spatiotemporal thermal profiles (<0.5% relative error in pertinent time scales) along with salient computational acceleration (up to two orders of magnitude speed-up) over the full-scale analysis. These findings establish the feasibility of ROM to perform rational and computationally affordable thermal analysis, develop reliable thermal control strategies for spacecraft, and greatly reduce the development cycle times and costs.

*Corresponding author
E-mail: yxw@cfdrc.com
Phone: +01-256-726-4915
Fax: +01-256-726-4806

1. INTRODUCTION

Computational models and analysis are increasingly used to support the engineering of spacecrafts at every stage of the development [1-4], including design, test, ground-operation simulation, and controller development. Every single element in the spacecraft needs to be thermally interrogated to ensure that its temperature, thermal distortion and stability remain in the pre-defined operating envelope and in-orbit performance requirements are met during all mission phases. Trends in recent years have been towards larger thermal models, and have therefore, placed additional computational demands on thermal engineers. Attempts to verify designs by modeling and analysis rather than testing further add to this burden.

Currently, there are three categories of models that are prevalently used in spacecraft thermal design: general thermal analytical models, approximate thermal analytical models [3, 5, 6], and heuristic models [7-9]. In general thermal analytical models, the discretized form of the governing PDEs for heat transfer, provide detailed and accurate temperature distributions in the spacecraft that can be used to resolve the thermal interaction with other physics for coupled analysis. Concurrently executed user logic and/or other customized inputs are typically used as the boundary conditions and heat sources. However, the computational process of general models normally is computationally intensive and time-consuming, which could take anywhere from days to weeks to yield reasonable answers to design questions. In contrast, approximate models based on the lumped-parameter assumption allows fast simulation speed and the ability to interrogate critical physics by parametric, tradeoffs, and interface studies at an early stage of the thermal design when the spacecraft concept, structure, and test arrangement are yet fully defined. Therefore, it provides valuable information about the feasibility of the spacecraft from the thermal perspective [6]. However, approximate models are generally poor in accuracy and lack quantitative predictive capability. More importantly, existing approximate thermal models are not capable of providing detailed temperature distribution in spatial domains; therefore they are inapplicable to coupled, multi-disciplinary spacecraft analysis.

To overcome aforementioned limitations, data-driven heuristic models have been developed for rapid parametric analysis and design evaluation. Miller [7, 10, 11] used the response surface methodology to study the thermal performance of the Orion vehicle with varying attitudes. The model showed good agreement with the general thermal analytical models and quickly screened a large number of verification tasks. Prince [9] derived response surface equations from the high-fidelity thermal model of the Mars Reconnaissance Orbiter and integrated those equation into the autonomous aerobraking simulation software. A goodness of fit analysis was performed confirming the response surface equations adequately represented the high-fidelity thermal model. However, issues associated with data driven heuristic models include: (1) they are the regression-based method, leading to poor accuracy relative to the mathematically rigorous, general thermal models, (2) the regression mapping is established between the input parameters and point-wise quantities of interest (e.g., max/min at critical locations), and hence, cannot be used to predict the entire spatial temperature distribution within the spacecraft; and (3) in general, they are ill-suited for predicting the dynamic thermal behavior of the spacecraft. Therefore, there is a strong need for an efficient spacecraft thermal modeling and analysis methodology that enables salient analysis accuracy similar to high-fidelity general thermal models but costs a fraction of their simulation time (equivalent to the approximate or heuristic models).

In this context, this paper presents a generalized, mathematically formal, subspace projection-based reduced order modeling (ROM) methodology for spacecraft thermal analysis. The computationally efficient ROM is automatically derived by projecting a full-scale general thermal model onto a low-dimensional, characteristic subspace. Two rigorous algorithms used to construct the subspace, including proper orthogonal decomposition (POD) [12-15] and trajectory piecewise linear reduced order modeling (TPWL-ROM) [16-19] are presented, and their formulation specific to spacecraft thermal model is described. As a result, a low-dimensional ROM whose size is 1-2 orders of magnitude less than the

original full-scale model can be obtained. The ROM is then coupled with ordinary differential equation (ODE) and differential algebraic solver (DAE) solvers to resolve the spatiotemporal temperature profile of the whole spacecraft. The ROM is verified against the full-scale, general thermal models of the spacecraft, including the Laser Interferometer Space Antenna (LISA) satellite and the Global Precipitation Measurement (GPM) satellite model available at the NASA Goddard Space Flight Center.

The facets that clearly distinguish the present work from the existing efforts include: (1) the first attempt to develop ROMs for spacecraft thermal analysis based on the mathematically rigorous, subspace projection method; (2) our ROMs bridge the gap among the existing techniques, and saliently combine several benefits of them in terms of computational accuracy and speed. Different from the approximate and heuristic model, our ROM is capable of capturing the entire temperature profile within the spacecraft in a transient manner, and allows for comprehensive spatiotemporal inspection of the thermal transport at the system level. Relative to the full-scale general thermal model, typically 1-2 orders of magnitude dimension reduction and computational speedup can be achieved without appreciably compromising simulation accuracy. The judicious combination of these merits make ROM-based simulation methodology well-suited for initial concept evaluation and screening, orbital analysis, operational optimization, as well as development of reliable thermal management strategies; and (3) in addition to the ROM algorithms, the present paper also formulates a systematic approach for acquiring and converting full-scale models in complex scenarios (e.g., temperature dependent parameters) to the form amenable to ROM implementation, laying a firm foundation for subsequent development.

The paper is organized as follows: the ROM approach and procedure is first introduced in Section 2, in which the acquisition of the full scale model and the POD and TPWL algorithms are elucidated. In Section 3, the ROMs are verified and demonstrated using two relevant satellite model examples. The paper is finally summarized in Section 4.

2. ROM METHODOLOGY

In this section, we will first present the systematic organization of the ROM methodology for spacecraft thermal analysis. Then the key elements of the full-scale model acquisition and dimension reduction for generating reduced thermal models will be described. As shown in Figure 1, the ROM-based thermal analysis includes three key steps:

1. Acquisition of full-scale, general thermal models: The first step is to import the definitive information of the spacecraft model from relevant thermal analysis software into the ROM platform via an external interface. The information includes conductive and radiative links, node capacitance, environment sources, user sources, etc. obtained from appropriate differencing schemes (e.g., finite difference or finite element). The model information is then assembled to form a set of ODEs/DAEs in compliance with the energy conservation on each node and the connectivity among nodes. The ODE/DAE set hence represents the full-scale, general thermal models that can be computed to predict the temperature distribution in a transient manner. More details are provided in Section 2.1.
2. Generation of reduced order model: The assembled full-scale thermal model is then reduced using the mathematically rigorous ROM algorithm. Specifically, a low-dimensional subspace is constructed, onto which the full-scale model is projected leading to a low-dimension thermal ROM. The ROM can be integrated using ODE/DAE solvers to resolve the transient temperature profile in the reduced domain. Due to its significantly reduced dimension relative to the full model, the ROM can be computed quickly and efficiently. The results of the generated ROM can then be compared against the full-scale thermal model for verification. More details are provided in Section 2.2.
3. Use of ROMs for spacecraft thermal analysis: It should be noted that in many instances, ROM generation is a one-time cost, and the validated ROM can be reused in subsequent iterative simulation sweeping the operating parameter space to identify the best parameter combination for design optimization and thermal control strategy. In contrast to the heuristics-based approach that establishes

the point-wise input-output mapping, the projection-based ROM bears excellent accuracy in the parameter space to predict the entire dynamic temperature distribution because of its mathematically rigorous nature. More details are provided in Section 3.

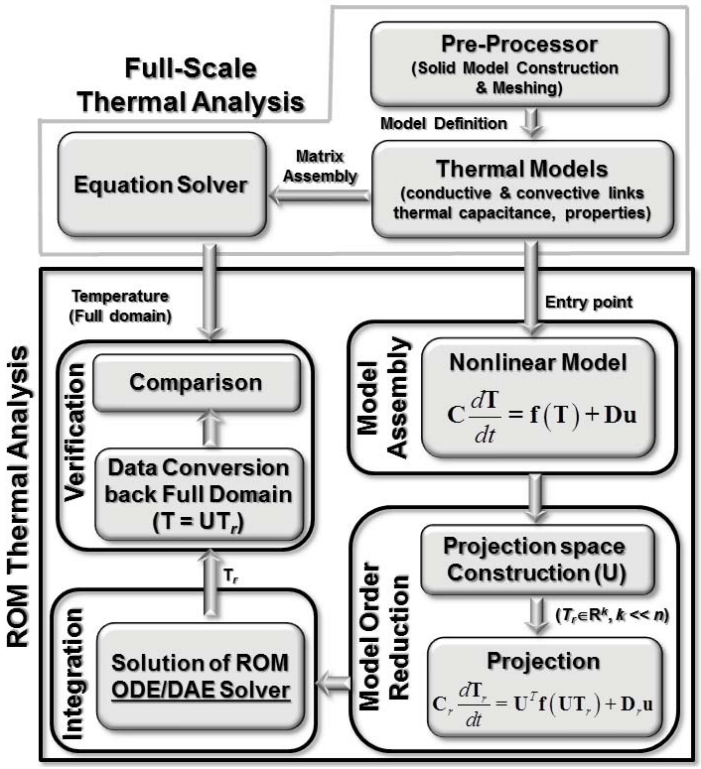

Figure 1. Schematic of the ROM methodology for spacecraft thermal analysis. Model definitive information is obtained from the full-scale model via an external interface. The imported model is assembled and reduced using mathematically rigorous algorithms to obtain the reduced order model. Both full-scale and ROM models are solved and the ROM performance characterized in terms of computational speedup and accuracy. Note that due to the use of projection methods the comparison between ROM and full-scale model is made over the entire spatiotemporal domain.

2.1 Acquisition of Full-scale Thermal Models

The procedure starts with acquisition of the full-scale thermal model. First, a custom interface is used to import the definitive information (such as thermal links, heat sources, thermal capacitance, etc.) from the geometrical mathematical model provided by the commercially available full-scale thermal analysis tool. Next model information is assembled into a dynamic ODE/DAE system governing the heat transfer at each individual node (or element depending on the discretization schemes used) in the spacecraft along with appropriately selected system inputs

$$C_i \frac{\partial T_i}{\partial t} = -\left(\sum_j^{N_i} K_{ij}\right) T_i + \left(\sum_j^{N_i} K_{ij} T_j\right) - \left(\sum_j^{M_i} R_{ij}\right) T_i^4 + \left(\sum_j^{M_i} R_{ij} T_j^4\right) + K_{si}\left(T_s - T_i\right) + R_{si}\left(T_s^4 - T_i^4\right) + Q_i \tag{1}$$

where T_i, C_i, and Q_i are, respectively, the temperature, thermal capacitance, and heat source of the i^{th} node (i=1, 2…n) and n is the total number of the node. Note that Q_i includes heat sources from internal heat generation (e.g., heaters and electronics heat dissipation) as well as environmental fluxes (e.g., direct solar radiation, albedo and earth radiation) [6]; K_{ij}, R_{ij}, are, respectively, the conductive and radiative links between nodes. N_i and M_i are, respectively, the number of the neighboring node interacting with the i^{th}

node via conduction and radiation. K_{si} and R_{si} are the conductive and radiative links between the i^{th} node and an isothermal object (e.g., space), respectively. T_s is the temperature of the isothermal object. Eq. (1) can be cast into a compact matrix form containing all nodes:

$$\mathbf{C}\frac{\partial \mathbf{T}}{\partial t} = \mathbf{AT} + \mathbf{RT}^{*4} + \mathbf{A}_s\mathbf{T}_s + \mathbf{R}_s\mathbf{T}_s^{*4} + \mathbf{Q} \tag{2}$$

where $\mathbf{T}\in\Re^n$ is a column vector containing the temperature at all nodes; $\mathbf{T}_s$ is the temperature of the isothermal object. $\mathbf{C}\in\Re^{n\times n}$ is the thermal capacitance matrix with the node-wise values C_i on its diagonal. $\mathbf{A}\in\Re^{n\times n}$ and $\mathbf{R}\in\Re^{n\times n}$ is the conduction and radiation exchange matrices, respectively, filled with the values of the conductive and radiative conductors in the model. $\mathbf{A}_s\in\Re^{n\times n}$ and $\mathbf{R}_s\in\Re^{n\times n}$ are matrices storing the conductive and radiative links between the nodes and the isothermal objects (see Appendix for additional details). The superscript of *4 means the 4th power is applied to each element of a vector. $\mathbf{Q}\in\Re^n$ is heat flux to each node. Since the heat flux $\mathbf{Q}$ can be split into constant flux $\mathbf{Q}_{const}$ and time varying flux $\mathbf{Q}_t$, we can define

$$\mathbf{Q}_c = \mathbf{A}_s\mathbf{T}_s + \mathbf{R}_s\mathbf{T}_s^{*4} + \mathbf{Q}_{const}, \quad \mathbf{Q}_t = \mathbf{Du} \tag{3}$$

i.e., $\mathbf{Q}_c$ stores the constant thermal contribution from the isothermal objects and others ($\mathbf{Q}_{const}$) on the nodes. Thus Eq. (2) can be rewritten as

$$\mathbf{C}\frac{d\mathbf{T}}{dt} = \mathbf{AT} + \mathbf{RT}^{*4} + \mathbf{Q}_c + \mathbf{Du} \tag{4}$$

where $\mathbf{u}$ and $\mathbf{D}$ are, respectively, the independent inputs and the scatter matrix that converts the time-varying flux into thermal source to each node, such as the logic-controlled heaters and environmental heat flux.

2.2 Reduced Order Modeling Algorithms

Since the dimension of Eq. (2) is normally too large for efficient numerical integration, the ROM technique will be used to reduce the original full-scale model with a dimension n to a much lower dimension k by projecting the original model onto a low-dimensional subspace $\mathbf{U}\in\Re^{n\times k}$ (i.e., $\mathbf{T} = \mathbf{UT}_r$) constructed by a set of orthonormal basis vectors, where $\mathbf{T}_r\in\Re^k$ is the temperature in the reduced domain and $k << n$. Herein, we present two mathematically rigorous ROM algorithms, i.e., proper orthogonal decomposition (POD) and trajectory piecewise-linear (TPWL) reduced order modeling to identify an appropriate, low-dimensional projection subspace and automatically generate reduced thermal models amenable to fast computation by ODE/DAE solvers.

Proper Orthogonal Decomposition Reduced order modeling (POD-ROM)

Proper orthogonal decomposition (POD) [20] is a powerful method for data reduction and ROM, and has been extensively investigated for nonlinear dynamic systems, such as the rapid thermal processing systems [12, 13]. Therefore, it is an exceptional candidate to address strong nonlinear effects in spacecraft thermal analysis. For POD implementation, the method of snapshots is used, which extracts the subspace consisting of leading POD modes using an ensemble of data (snapshots) from the computation of the original, full-scale model [21]. To provide high-quality snapshot data, it is necessary to choose temporally characteristic, orbital input functions u (typically a series of sequences with relevant time scales) for the full-scale analysis. Given an input u, the matrix $\mathbf{\Gamma}$ containing the temperature snapshots at certain instances of time t_l is given by

$$\mathbf{\Gamma} = \left[\mathbf{T}(t_1)\,\mathbf{T}(t_2)\cdots\mathbf{T}(t_l)\cdots\mathbf{T}(t_N)\right] \tag{5}$$

where $\mathbf{T}(t_l)$ is the l^{th} snapshot in time; $l = 1,2\ldots N$ and N is the total number of the snapshots. $\mathbf{\Gamma}$ then can be factorized using the singular value decomposition (SVD), followed by truncation at the first $k << n$ leading modes yielding

$$\mathbf{\Gamma} \approx \mathbf{U}\sum\mathbf{V}^T \tag{6}$$

where $\mathbf{U} \in \Re^{n \times k}$ is the dominant subspace comprised of the k leading POD modes spanning the original snapshot matrix, $\mathbf{\Sigma} \in \Re^{k \times k} = \text{diag}\{\sigma_i\}$ is a diagonal matrix of singular values arranged in a descending order. The singular value σ_i measures the dominance of its associated column in $\mathbf{U}$. Therefore, by examining the relative magnitude of σ_i, an appropriate number k can be determined for ROM that yields desired model accuracy; and $\mathbf{V} \in \Re^{N \times k}$ is the mode in the temporal domain. The original full-scale model Eq. (4) then can be projected onto the subspace $\mathbf{U}$ yielding a reduced thermal model with a much lower dimension (i.e., $k << n$):

$$\mathbf{C}_r \frac{d\mathbf{T}_r}{dt} = \mathbf{A}_r \mathbf{T}_r + \mathbf{R}_r \left(\mathbf{U}\mathbf{T}_r\right)^{*4} + \mathbf{Q}_{cr} + \mathbf{D}_r \mathbf{u} \tag{7}$$

where $\mathbf{C}_r = \mathbf{U}^T \mathbf{C} \mathbf{U}$, $\mathbf{A}_r = \mathbf{U}^T \mathbf{A} \mathbf{U}$, $\mathbf{R}_r = \mathbf{U}^T \mathbf{R}$, $\mathbf{Q}_{cr} = \mathbf{U}^T \mathbf{Q}_c$, $\mathbf{D}_r = \mathbf{U}^T \mathbf{D}$, $\mathbf{T}_r = \mathbf{U}^T \mathbf{T}$. Given its significantly lower dimension, the ROM governing $\mathbf{T}_r$ can be computed at much faster speed relative to the full-scale model using ODE/DAE solver. Figure 2 illustrates the flow chart of POD-ROM methodology.

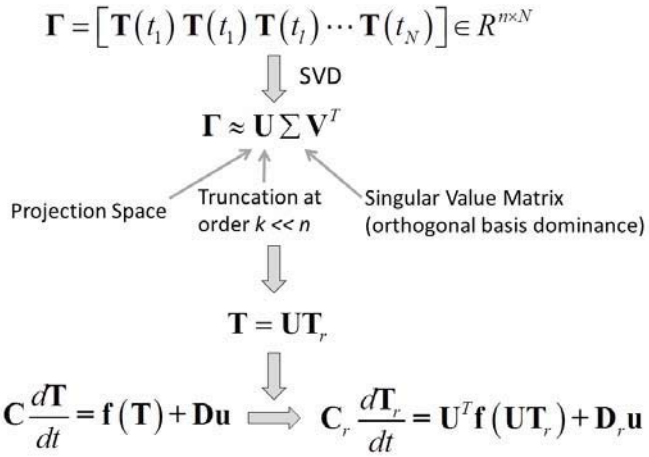

Figure 2. POD-based ROM algorithm development for spacecraft model. Snapshots from the full-scale model are factorized using singular value decomposition, followed by truncation at k leading modes, such that the ROM dimension k is significantly smaller than the full-scale model dimension n.

Although POD is simple and accurate, its computational efficiency can be limited by the fact that the calculation of the nonlinear term $\mathbf{T}^{*4}$ requires converting the solution $\mathbf{T}_r$ in the reduced domain back to the full domain $\mathbf{T}$ (as shown in Eq. (7)) and calculating the 4th order power of $\mathbf{T}$ on all nodes, leading to appreciable burden for computational acceleration (in particular for large models). To alleviate this issue, the discrete empirical interpolation method (DEIM) [22-24] can be used to approximate the nonlinear terms directly using the variable $\mathbf{T}_r$ in the reduced domain, and hence, improves the computational efficiency. DEIM constructs specially selected interpolation indices that identify an interpolation-based projection to provide a nearly optimal subspace approximation to the nonlinear term. Therefore, only a few entries of the original nonlinear terms selected by the DEIM need to be evaluated at each time step. In DEIM, the nonlinear term is projected onto another subspace $\mathbf{W} \in \Re^{n \times q}$ with $q << n$, which in our case implies

$$\mathbf{T}^{*4} \approx \mathbf{W}\mathbf{H} \tag{8}$$

where $\mathbf{W}$ can be obtained using POD on the snapshot data of the nonlinear term only (i.e., $\mathbf{T}^{*4}(t_1)$, $\mathbf{T}^{*4}(t_2)$,…$\mathbf{T}^{*4}$ (t_l),…$\mathbf{T}^{*4}(t_N)$ used in Eq. (5) instead). $\mathbf{H} \in \Re^q$ is the corresponding coefficient vector to be determined. Denote $\mathbf{P} \in \Re^{n \times q}$ a matrix composed by q selected columns from the identity matrix $\mathbf{I} \in \Re^{n \times n}$, i.e., $\mathbf{P} = \left[\mathbf{e}_{\aleph 1}, \cdots, \mathbf{e}_{\aleph q}\right]$. If $\mathbf{PW}$ is nonsingular, the coefficient vector $\mathbf{H}$ can be determined from $\mathbf{P}^T\mathbf{T}^{*4}$ =

$\mathbf{P}^T\mathbf{WH}$. Thus approximation to Eq. (8) becomes

$$\mathbf{T}^{*4} \approx \mathbf{W}\left(\mathbf{P}^T\mathbf{W}\right)^{-1}\mathbf{P}^T\mathbf{T}^{*4} = \mathbf{W}\left(\mathbf{P}^T\mathbf{W}\right)^{-1}\left(\mathbf{P}^T\mathbf{T}\right)^{*4}. \tag{9}$$

The transformation in Eq. (9) allows the computation of the nonlinear terms only on a small number of selected nodes that have salient thermal contributions. Thus the reduced system of Eq. (7) can be modified as

$$\mathbf{C}_r\frac{d\mathbf{T}_r}{dt} = \mathbf{A}_r\mathbf{T}_r + \mathbf{R}_r\mathbf{W}\left(\mathbf{P}^T\mathbf{W}\right)^{-1}\left(\mathbf{P}^T\mathbf{U}\mathbf{T}_r\right)^{*4} + \mathbf{Q}_{cr} + \mathbf{D}_r\mathbf{u} = \mathbf{A}_r\mathbf{T}_r + \hat{\mathbf{R}}_r\left(\hat{\mathbf{P}}\mathbf{T}_r\right)^{*4} + \mathbf{Q}_{cr} + \mathbf{D}_r\mathbf{u} \tag{10}$$

where $\hat{\mathbf{R}}_r = \mathbf{R}_r\mathbf{W}\left(\mathbf{P}^T\mathbf{W}\right)^{-1}$, and $\hat{\mathbf{P}} = \mathbf{P}^T\mathbf{U}$ can be pre-computed prior to the simulation. The interpolation indices $\aleph_1,\cdots,\aleph_q$ that construct the selection matrix $\mathbf{P}$ are selected inductively by the following algorithm [23]:

Input: $\left\{\mathbf{w}_1,\cdots,\mathbf{w}_q\right\}$

1. $\left[\rho\ \aleph_1\right] = \max\left(\left|\mathbf{w}_1\right|\right)$
2. $\mathbf{W} = \left[\mathbf{w}_1\right],\ \mathbf{P} = \left[\mathbf{e}_{\aleph_1}\right]$
3. loop l = 2 to q
   - Solve $\left(\mathbf{P}^T\mathbf{W}\right)\mathbf{Z} = \mathbf{P}^T\mathbf{w}_l$ for $\mathbf{Z}$
   - $\mathbf{r} = \mathbf{w}_l - \mathbf{W}\mathbf{Z}$
   - $\left[\rho\ \aleph_l\right] = \max\left(\left|\mathbf{r}\right|\right)$
   - $\mathbf{W} = \left[\mathbf{W}\ \mathbf{w}_l\right],\ \mathbf{P} = \left[\mathbf{P}\ \mathbf{e}_{\aleph_l}\right]$
4. End loop

Output: **P** for nonlinear function projection

Figure 3. Algorithm for the discrete empirical interpolation method (DEIM)

The function of "max" in the above algorithm returns the maximum component ρ in a vector along with the corresponding index of $\aleph_l$. The process of the DEIM may be interpreted as selecting the indices of most representative components for approximating the nonlinear term [25].

Trajectory Piecewise-Linear Reduced order modeling (TPWL-ROM)

Another effective means to address the nonlinear terms in ROM is to use the trajectory piecewise-linear (TPWL) technique [17, 18, 26-28]. That is, the full-scale nonlinear thermal model is first linearized along a series of linearization points. The TPWL approximation is utilized to construct a weighted combination of the linearized models to mimic the behavior of the original, full-scale nonlinear system in the entire domain. The linearized full-scale models in the weighted combination are then reduced to linearized ROMs using the subspace project method above. Specifically, the nonlinear thermal equation in Eq. (4) can be cast into a more compact form as

$$\mathbf{C}\frac{d\mathbf{T}}{dt} = \mathbf{f}\left(\mathbf{T}\right) + \mathbf{D}\mathbf{u} \quad \text{and} \quad \mathbf{f}\left(\mathbf{T}\right) = \mathbf{A}\mathbf{T} + \mathbf{R}\mathbf{T}^{*4} + \mathbf{Q}_c \tag{11}$$

$\mathbf{f}(\mathbf{T})$ includes the conductive and radiative heat flux as well as the constant heat sources, and can be approximated using the Taylor expansion about a certain temperature $\mathbf{T}_i$,

$$\mathbf{f}\left(\mathbf{T}\right) \approx \mathbf{f}\left(\mathbf{T}_i\right) + \mathbf{h}\left(\mathbf{T}_i\right)\left(\mathbf{T} - \mathbf{T}_i\right) \tag{12}$$

where $\mathbf{h}(\mathbf{T}_i)$ is the Jacobian of $\mathbf{f}(\mathbf{T})$ evaluated at $\mathbf{T}_i$ while $\mathbf{T}_i$ is the i^{th} linearization point, *i = 1, 2, ..., s*. Note that substitution of Eq. (12) back into Eq. (11) yields a linearized full-scale model at the proximity

of $\mathbf{T}_i$. The original, full nonlinear model is then approximated by combining all the linearized models at the linearization points using TPWL method, i.e.,

$$\mathbf{C}\frac{d\mathbf{T}}{dt} = \sum_{i=1}^{s} \omega_i \left[\mathbf{f}(\mathbf{T}_i) + \mathbf{h}(\mathbf{T}_i)(\mathbf{T} - \mathbf{T}_i) + \mathbf{D}\mathbf{u} \right] \tag{13}$$

where ω_i is the normalized temperature-dependent weight and $\sum_{i=1}^{s} \omega_i = 1$. Although linearized, direct computation of Eq. (13) is typically prohibitive due to its large dimension. Thereby a ROM procedure is normally taken to reduce its size, which is given as follows: determining a local projection subspace $\mathbf{U}_i$ at each linearization point in a trajectory/training simulation using a linear ROM technique (e.g., the Krylov-subspace ROM [29]). Then, an SVD is applied onto the union of all $\mathbf{U}_i$ to extract the global projection subspace $\mathbf{U} \in \Re^{n \times k}$, where k again denotes the reduced dimension. Alternatively, the global projection space can also be obtained by directly applying POD/SVD on the snapshots obtained from the training/trajectory simulation. Based on our experience, the global subspace $\mathbf{U}$ obtained by the latter exhibits enhanced accuracy and robustness while the former allows subspace determination without resorting to full-scale model computation. Finally Eq. (13) is projected onto the global subspace $\mathbf{U}$ yielding:

$$\mathbf{C}_r \frac{d\mathbf{T}_r}{dt} = \sum_{i=1}^{s} \omega_i \mathbf{h}_r(\mathbf{T}_i)\mathbf{T}_r + \omega_i \left[\mathbf{f}_r(\mathbf{T}_i) - \mathbf{h}_r(\mathbf{T}_i)\mathbf{T}_{ir} \right] + \omega_i \mathbf{D}_r \mathbf{u} \tag{14}$$

where $\mathbf{f}_r(\mathbf{T}_i)=\mathbf{U}^T\mathbf{f}(\mathbf{T}_i)$, $\mathbf{h}_r(\mathbf{T}_i)=\mathbf{U}^T\mathbf{h}(\mathbf{T}_i)$. Eq. (14) is essentially a weighted combination/interpolation of the linearized ROMs. The weights ω_i in Eq. (14) depend on the temperature of each node during the simulation, and can be calculated by the algorithm based on the Euclidean distance [17] as shown in Figure 4. Figure 5 illustrates the flow chart of the TPWL-ROM to generate reduced thermal models for spacecraft thermal analysis.

1. For $i = 1,\ldots s$ compute $d_i = \|T\text{-}T_i\|_2$.
2. Take $m = \min(d_i)$ for $i = 1,\ldots s$.
3. For $i = 1,\ldots s$ compute $w_i = e^{-\lambda di/m}$.
4. Normalize w, set $\omega_i = w_i \Big/ \sum_{j=1}^{s} \omega_j$

Figure 4. Algorithms to calculate the interpolation weights ω_i for TPWL-ROM

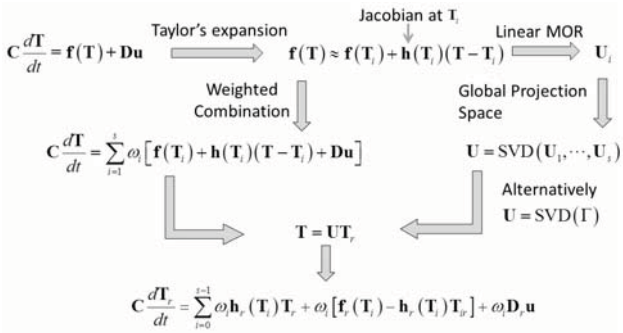

Figure 5. Flow chart of TPWL-ROM

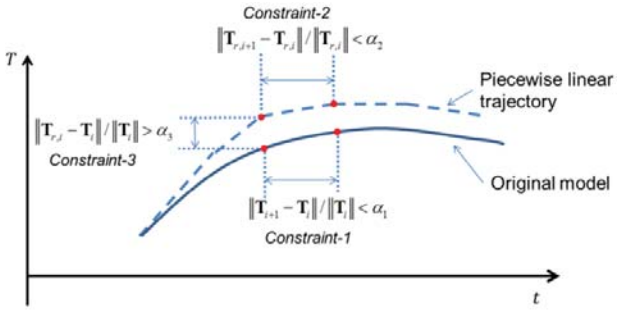

Figure 6. Three different methods to locate the linearization points $\mathbf{T}_i$.

An open question with TPWL-ROM is how to determine linearization points along a representative trajectory to accurately capture the dynamic response of the system. As illustrated in Figure 6, in general there are three methods to locate the linearization points. The first one (*Constraint*-1) uses a step-size constraint based on the simulation of the full-scale model, that is, the step size between two linearization

points ($\mathbf{T}_i$ and $\mathbf{T}_{i+1}$) needs to be below a tolerance $\|\mathbf{T}_{i+1} - \mathbf{T}_i\|/\|\mathbf{T}_i\| < \alpha_1$. In the second approach (*Constraint-2*), the step size is calculated using the linearized ROM and is restricted by $\|\mathbf{T}_{r,i+1} - \mathbf{T}_{r,i}\|/\|\mathbf{T}_{r,i}\| < \alpha_2$. The third approach is essentially an error constraint (*Constraint-3*), where the excursion from one linearization point to the next is determined in such a way that the error between the original full model and ROM is bounded, i.e., $\|\mathbf{T}_{r,i} - \mathbf{T}_i\|/\|\mathbf{T}_i\| < \alpha_3$, and hence, it requires the computation of both full-scale nonlinear and linearized ROM during the trajectory simulation. In this paper, the first and third constraints were utilized to locate the linearization points, and they typically took a value of 0.05–0.1.

3. RESULTS AND DISCUSSION

In this section, case studies using NASA-relevant spacecraft thermal analysis will be presented for ROM verification and demonstration. The original spacecraft thermal models in the form of the input data deck were exported from SINDA/FLUINT (S/F) [30], a widely used software tool in the spacecraft thermal analysis community. The S/F input data deck was then parsed using an in-house parser to extract pertinent model information and features, including: (1) nodal and inter-node information, such as capacitance and initial temperatures, conductive and radiative links/conductors, as well as the environmental and internal heating loads; (2) creating global indices for all nodes in various sub-models and for the nodal interactions; and (3) control logics used in the S/F model. The information parsed from the S/F model was then assembled in the form of Eq.(4), which, hence, is termed full-scale model hereafter. To quantitatively characterize the discrepancy between the full-scale model and ROM, two performance indices were used: the absolute error and the relative root mean square (rms) error, which are given by

$$Err_{abs} = \mathbf{U}\mathbf{T}_r - \mathbf{T} \quad \text{and} \quad Err_{rms} = \sqrt{\|\mathbf{U}\mathbf{T}_r - \mathbf{T}\|/\|\mathbf{T}\|} \tag{15}$$

where $\mathbf{T}_r$ and $\mathbf{T}$ are the absolute temperature data from the ROM and the full-scale model. Note that at each time step Err_{abs} is a vector and represents the temperature difference on all the nodes, while Err_{rms} is a scalar obtained by applying the L2-norm onto all the nodes in the model and indicates average relative error in the entire computational domain. To facilitate the comparison on the computational efficiency, both the full-scale model and ROM were simulated on the same platform, a Linux-based multi-user server equipped with 2 X AMD Opteron 6238 Twelve-Core 2.6GHz processor and 256 GB memory. The case studies using two spacecraft thermal models, Laser Interferometer Space Antenna (LISA) and Global Precipitation Measurement (GPM) with different computational sizes were analyzed.

3.1 Laser Interferometer Space Antenna (LISA) Model

The LISA mission, a space-based gravitational wave detector in the 0.1 to 1 mHz frequency band, measures distance fluctuations between proof masses aboard three spacecrafts. The LISA Integrated Modeling team developed a detailed thermal model that was used to drive the design of LISA [31, 32]. In this paper, a LISA thermal model containing 2874 nodes was used. In the transient analysis, the solar frequency is set at 0.1 mHz with 1% fluctuation in solar intensity (around the steady-state values). The overall heat source terms are given as

$$\mathbf{Q}_c = \mathbf{Q}_{elec} \quad \text{and} \quad \mathbf{Q}_t = \mathbf{D}u_0\left(1 + \sin\left(2\pi\omega t\right)\right)$$

where $\mathbf{Q}_{elec}$ is the electronics heating and $\mathbf{Q}_t$ is the heat input from the solar radiation; u_0 and ω are, respectively, the amplitude and frequency of the sinusoidal solar input.

The model verification was undertaken in two steps: (1) comparing the S/F data from NASA against the full-scale model results to verify our in-house parser; and (2) comparing the full-scale model with ROM results to demonstrate salient computational efficiency achieved by ROM. Note that since the computational platform employed in (2) is different from that in NASA on which S/F analysis was performed, a direct comparison between S/F vs. ROM in terms of computational time and speed is not available. Figure 7 illustrates the transient temperature profile of all the nodes obtained using the full-

scale model and the S/F data from NASA with $\omega = 0.1$ mHz to examine (1) above. The full-scale model exhibits excellent agreement with the S/F result in the entire spatiotemporal domain. The relative error Err_{rms} in the entire temporal domain is <0.007% as shown in Figure 7c. The absolute error Err_{abs} in the node-wise temperature and its temporal dependence is depicted in Figure 7d, which falls in the range of [-0.03K, 0.03K]. The temperature difference is negligible and may be caused by the different time stepping algorithms utilized by S/F and our full-scale model. Likewise, the transient simulation results with the solar frequency of $\omega = 1$ mHz are very similar (not shown here).

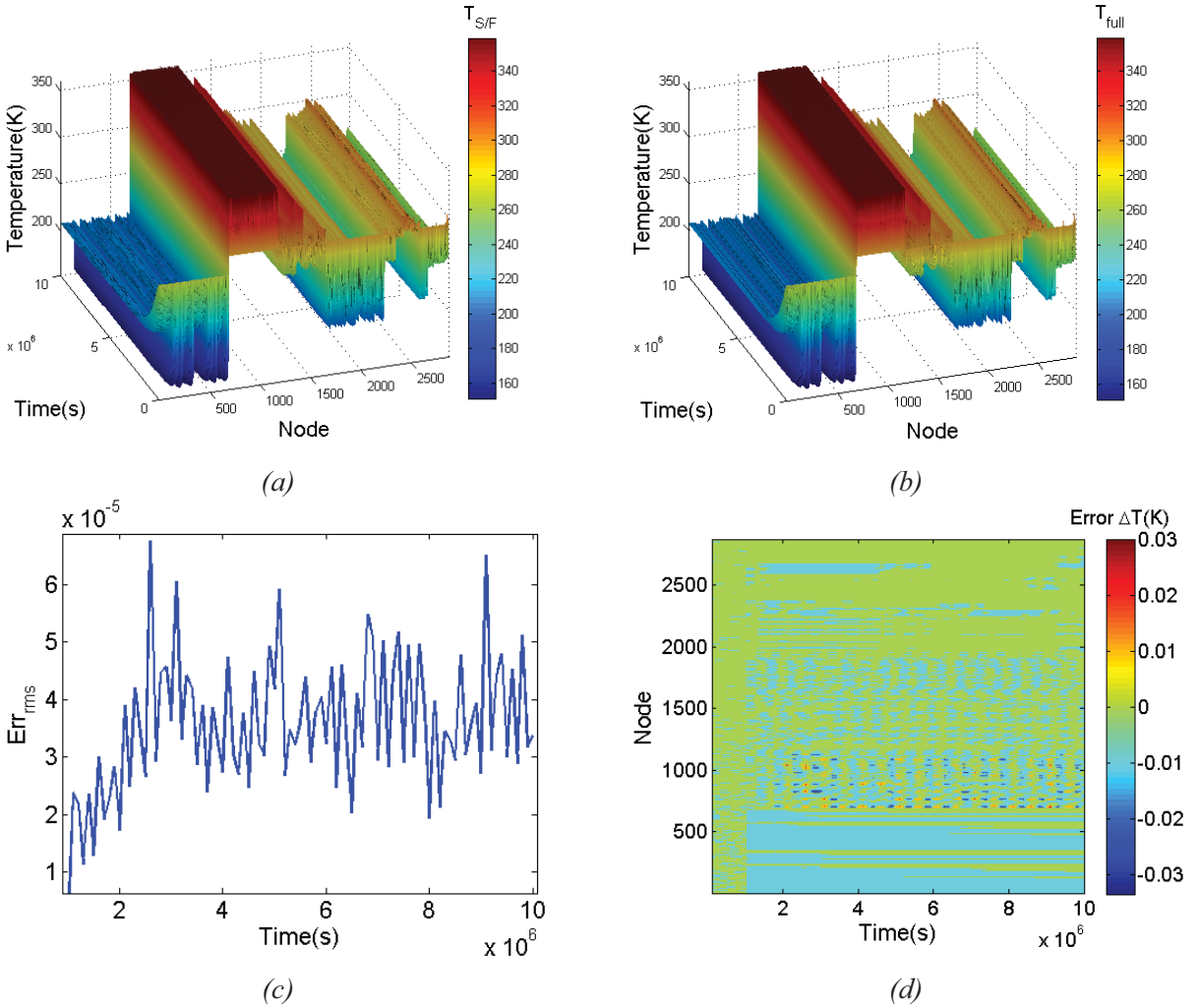

Figure 7. Comparison between the full-scale model and S/F results in transient temperature profile for the LISA model with a solar fluctuation frequency of 0.1 mHz: (a) S/F data; (b) Data from the full-scale model; (c) Relative error; and (d) Absolute error in the node-wise temperature values.

Next, the ROM is compared with the full-scale model in both accuracy and computational efficiency, i.e., step (2) above. In order to generate the snapshot data and ROM, trajectory simulation using appropriately selected training inputs that excite a broad spectrum of dynamic response in the nonlinear system were performed to determine the projection subspace **U**. The strategies to identify optimal inputs for snapshot simulation has been extensively discussed in prior research [33]. Normally it is an empirical process specific to individual systems, in particular, for complex environmental and heat source conditions (e.g., spacecraft). In our case study the training input is set as $\mathbf{u}_{train} = \mathbf{u}_0 f(t)$, where $\mathbf{u}_0$ is the constant solar radiation intensity and $f(t)$ is a time varying function [33] as shown in Figure 8.

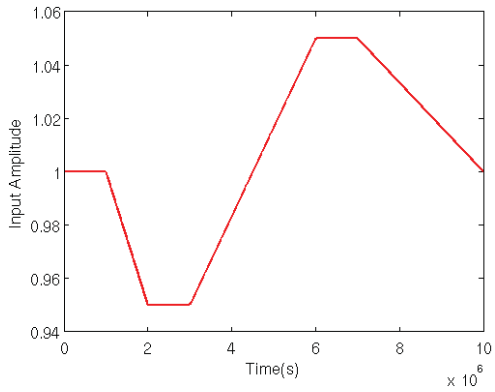

Figure 8. Training input profile (ramp function) for solar radiation in the LISA model.

POD-ROM

The training input in Figure 8 was used in the full-scale simulation to generate numerical snapshots and extract projection subspace, which took 324 seconds in total. A projection subspace **U** with a low dimension of $k = 12$ and DEIM projection space **W** in rank $q = 12$ were then obtained for ROM. It should be noted that the training simulation and subspace generation is a one-time cost for reusable ROM, and hence, is negligible for the situation where ROM needs to be repetitively computed for parametric analysis. In addition, the training cost also heavily depends on the selection of the input profile. Although a simpler input with a short period can greatly shrink the computational time but at the cost of narrower operating envelop and limited reusability. In this case study ROM obtained using the input profile in Figure 8 is broadly applicable to all the simulation conditions of our interest (e.g., different solar frequency and varying amplitude). Figure 9a illustrates the transient, node-wise temperature profile, which matches very well the S/F data and the full-scale model shown in Figure 7a-b. Figure 9b-c, and Table 1 show the absolute Err_{abs} and relative error Err_{rms} of the ROM as compared with the full-scale model solution, which are less than [-0.6K 0.6K] and 0.02%, respectively. For computational efficiency, the transient analysis using the full-scale model cost about 266 seconds, and the POD-ROM achieved a speedup of 216× over the full-scale model. These findings confirm that the projection space obtained from POD and associated nonlinear ROM is able to accurately capture the strongly nonlinear heat transfer in the LISA model.

Table 1. Computational performance for POD-ROM of the LISA model

ROM dimension	Err_{abs} (K)	Err_{rms} %	Speed-up
12	[-0.6 0.6]	< 0.02	216

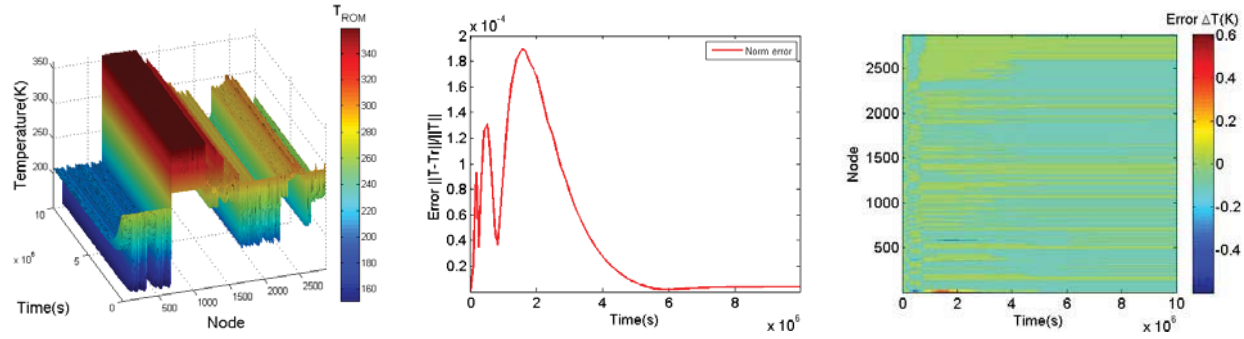

(a) *(b)* *(c)*

Figure 9. Simulation results of POD-ROM (k=12) vs. the full-scale LISA model: (a) Node-wise transient solution for ROM; (b) Relative error and (c) Absolute error.

TPWL-ROM

Next we present the TPWL-ROM results and its computational performance for the LISA model. Different schemes to locate the linearization points along the trajectory in the training simulation were investigated. Figure 10 and Table 2 illustrate the comparison of the TPWL-ROM using *constraint-1* (ROM_1) and *constraint-3* (ROM_3) against the full-scale model. The relative error Err_{rms} and absolute error Err_{abs} of the ROM_1 are, respectively, <0.02% and in the range of [-0.4K 0.6K]. For ROM_3, Err_{rms} is less than 0.06% and Err_{abs} falls between [-0.4K 1.2K]. Note that the transient temperature profile obtained using the TPWL-ROM is almost the same as that by POD-ROM, and hence, is not shown herein for sake of brevity. In terms of computational efficiency, ROM_1 and ROM_3 exhibit a speedup of 186× and 213×, respectively, in contrast to the full-scale model. The ROM_3 runs slightly faster than ROM_1 due to fewer linearization points than the former although both have the same dimensions.

Table 2. Computational performance for TPWL-ROM of the LISA model

	ROM_1, $\alpha = 0.1$			ROM_3, $\alpha = 0.05$		
ROM dimension	Err_{abs} (K)	Err_{rms} %	*Speed-up*	Err_{abs} (K)	Err_{rms} %	Speed-up
12	[-0.5 2]	< 0.08	186	[-0.5 1.5]	< 0.12	213

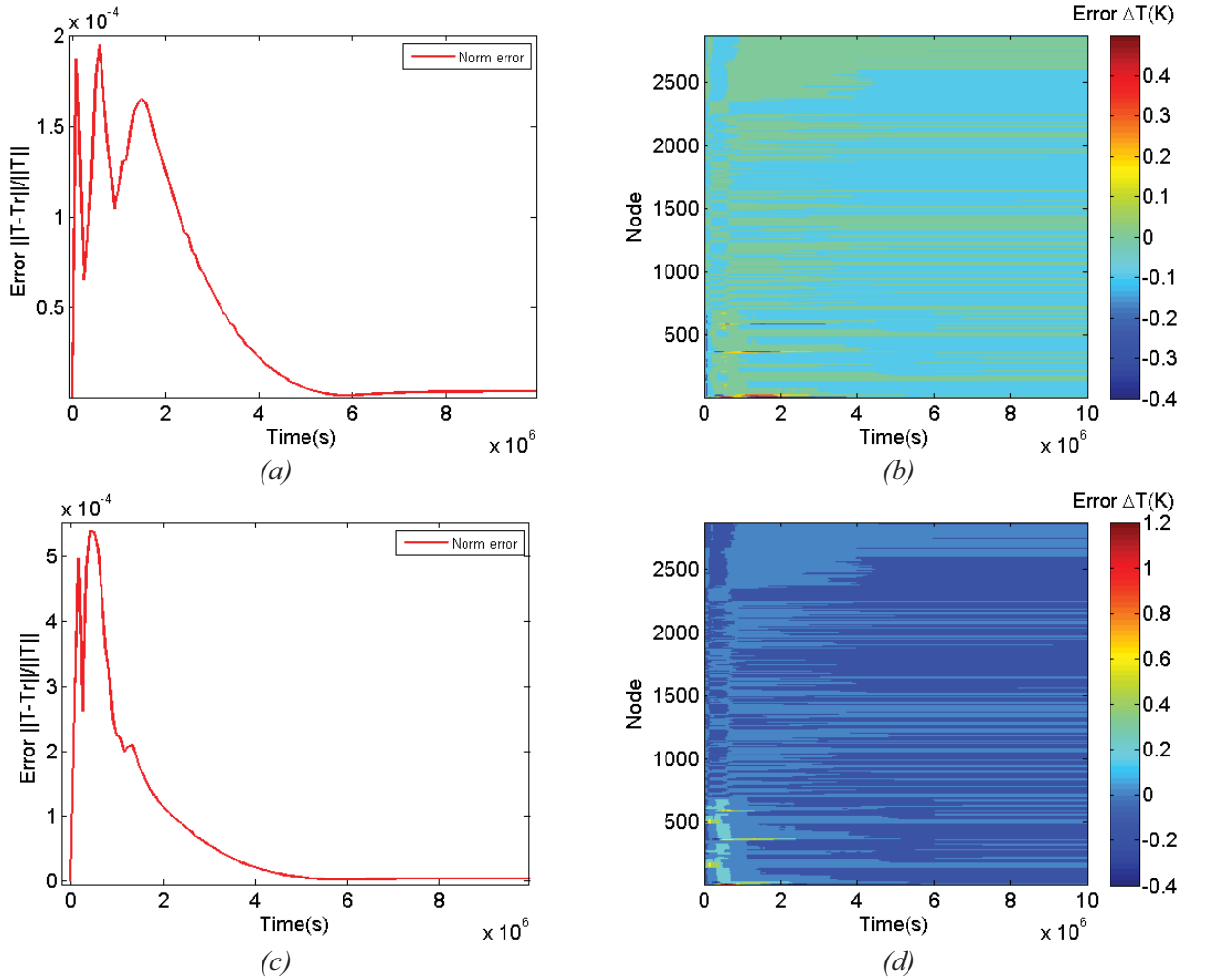

Figure 10. Simulation results of the TPWL-ROM (k=12) vs. the full-scale LISA model: (a, c) Relative error and absolute error, respectively, for ROM using Constraint-1 (ROM_1); (b, d) Relative error and absolute error, respectively, for ROM using Constraint-3 (ROM_3).

3.2 Global Precipitation Measurement (GPM) Model

The next case study is the in-orbit analysis of the GPM satellite model obtained from NASA. The GPM model carries several distinct features and poses significant challenges to both full-scale model analysis and ROM. It has a large model size, containing 44,233 nodes and more than 1,700,000 conductors. Many nodes are made of composite materials and have temperature dependent properties. A total number of ~10 orbits need to be simulated to eliminate the effect of the initial condition and examine its quasi steady-state thermal behavior.

The GPM model has more than 100 heaters with logic control, and their input power depend on the programmed control law and time. Therefore, it is unrealistic to configure training inputs for each individual heat source to generate snapshot data. This is made even challenging due to the discontinuous and irregular profiles of the environmental flux as shown in Figure 11. Instead, we divided the orbital analysis into two stages: at the first stage, the first 1-2 orbits of the GPM model were simulated using the full-scale model and the snapshots data was collected and used to determine the projection subspace **U** and the low-dimension ROM as well. At the second stage, the rest of the orbits were analyzed using the ROM. The underlying rationale is that the temperature solution at the second stage can be treated as the perturbation to those at the first stage, and hence, the projection subspace will be almost the same for both. However, it should be pointed out that in contrast to the LISA model above, it will be difficult to reuse the ROM obtained by this approach for other orbit analysis that may have heat source profile notably different from the snapshot simulations.

In the case study below, the first orbit of the full-scale GPM model was used as the snapshot data for subspace identification and ROM generation. The ROM was then used in the rest 9 orbits. In addition, our verification primarily focused on the comparison between extracted full-scale model and ROM with the S/F model neglected for two reasons: (i) the in-house parser has been verified extensively using the LISA and other relevant models; and (ii) the original GPM model in the S/F format from NASA included numerous heat pipes. However, HEATPIPE routines in S/F are not transparent to the external users, and cannot be parsed using our in-house tool at this stage.

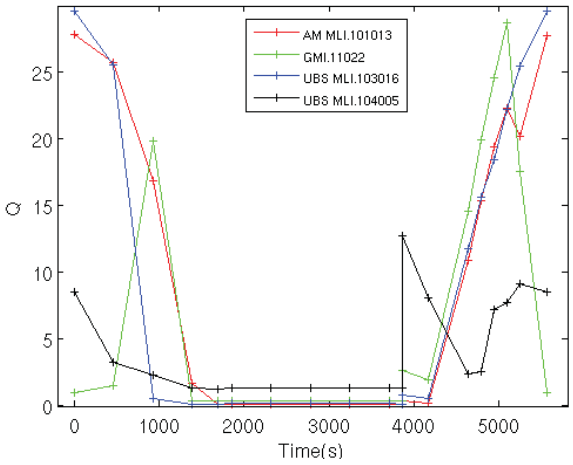

Figure 11. An example of environmental flux applied to several nodes in the GPM model shows profiles with dramatic changes and sharp spikes.

POD-ROM

The ROMs with a dimension of $k = 24$ and $k = 48$ were first generated using the POD method. Figure 12 portrays the transient node-wise temperature profiles obtained using the full-scale model and ROM with a dimension $k = 24$. The GPM model exhibits distinctly different thermal behavior at various regions as indicated by the dramatically oscillating temperature in some nodes while the rest remain almost constant due to strict thermal control requirements. As shown in Figure 13, the absolute Err_{abs} and relative error Err_{rms} is in the range of [-8K 8K] and less than 0.6% for the ROM with $k = 24$, respectively. However, as

the dimension increases to $k = 48$, the errors drop markedly, yielding $-4\text{K} \le Err_{abs} \le 4\text{K}$ and $Err_{rms} \le 0.4\%$. It is also interesting to note that Err_{abs} and relative error Err_{rms} slightly grow with the time for both ROMs. It is caused by the shift in the subspace spanning the temperature solution between the initial and subsequent orbits. The simulation time of the full-scale GPM model in the ten orbits is about 80337 seconds on our computational platform. The speedup of the ROM relative to the full-scale solutions is presented in two ways: the speedup was 9.8× and 9.2× if the computational cost of the snapshot simulation for the first orbit and the ROM generation was included. On the other hand, the speedup is 104× – 458× in the second to the tenth orbit without taking this cost into account [34], which confirms that the ROM simulation time is negligible in contrast to the full-scale model. The quantitative performance metrics for the POD-ROM is summarized in Table 3.

Table 3. Computational performance of POD in GPM model

ROM dimension	Err_{abs} (K)	Err_{rms} (%)	Speedup	
			10 orbits	2nd - 10th orbit
24	[-8 8]	< 0.6	9.8	458
48	[-4 4]	< 0.4	9.2	104

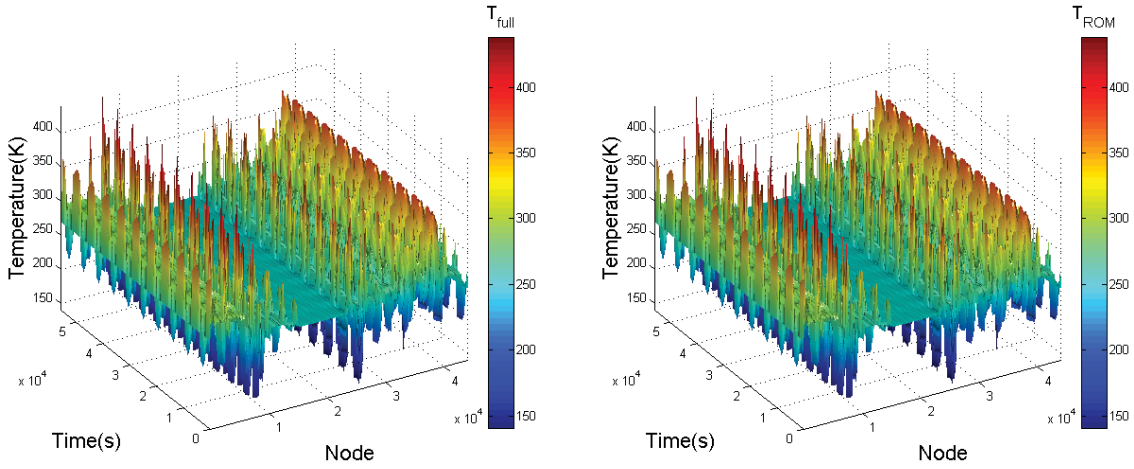

(a) *(b)*

Figure 12. Node-wise transient solution of GPM model: (a) generated by full-scale model; (b) POD-ROM of dimension 24.

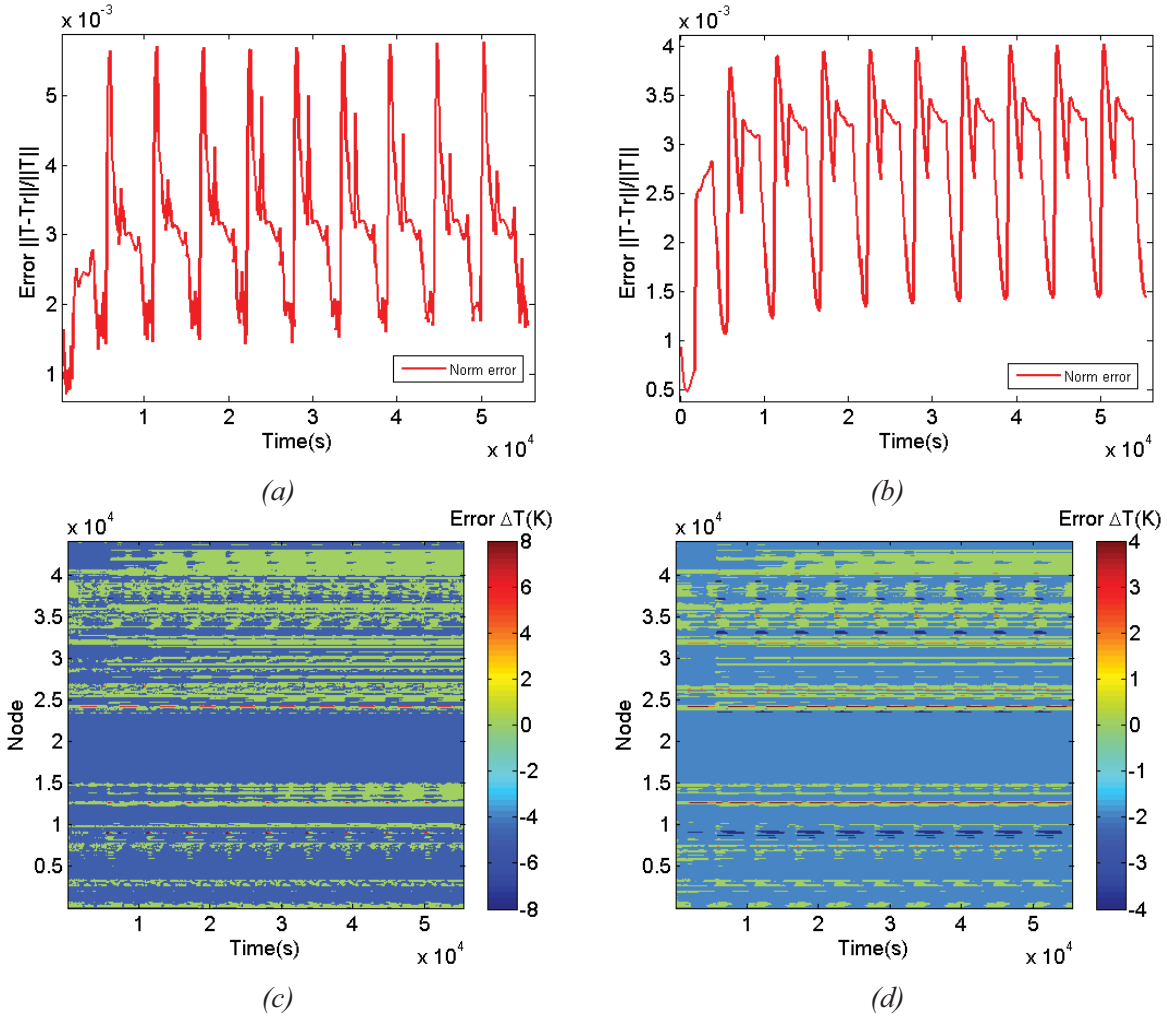

Figure 13. Simulation results of POD-ROM vs. the full-scale GPM model: (a, c) Relative error and absolute error, respectively, for the ROM with k = 24; and (b, d) Relative error and absolute error, respectively, for the ROM with k = 48.

TPWL-ROM

Table 4 and Figure 14 illustrate the comparison of the TPWL-ROM against the full-scale model solution using *constraint-1* (ROM_1) and *constraint-3* (ROM_3). For k = 24, the relative error Err_{rms} and the absolute error Err_{abs} are less than 0.8% and in the range of [-8 8K]. As the dimension increases to k = 48, Err_{abs} drops to [-5K 5K] and Err_{rms} becomes less than 0.4%. In terms of computational efficiency, ROM_1 demonstrates a speedup of 9.6× – 9.9× with and 216× – 642× without considering the cost associated with the initial snapshot simulation and ROM generation cost as discussed above. Correspondingly, ROM_3 exhibits a speedup of 9.5× – 9.8× with and 172× – 455× without the cost associated with initial snapshot simulation and ROM generation.

Table 4. Computational performance of TPWL-ROM for the GPM model

	ROM_1, α = *0.1*				ROM_3, α = *0.05*			
ROM dimension	Err_{abs} (K)	Err_{rms} %	Speed-up		Err_{abs} (K)	Err_{rms} %	Speedup	
			10 orbits	2nd - 9th orbit			10 orbits	2nd - 9th orbit
24	[-8 8]	< 0.8	9.9	642	[-8 8]	< 0.6	9.8	455

48	[-5 5]	< 0.4	9.6	216	[-5 5]	< 0.4	9.5	172

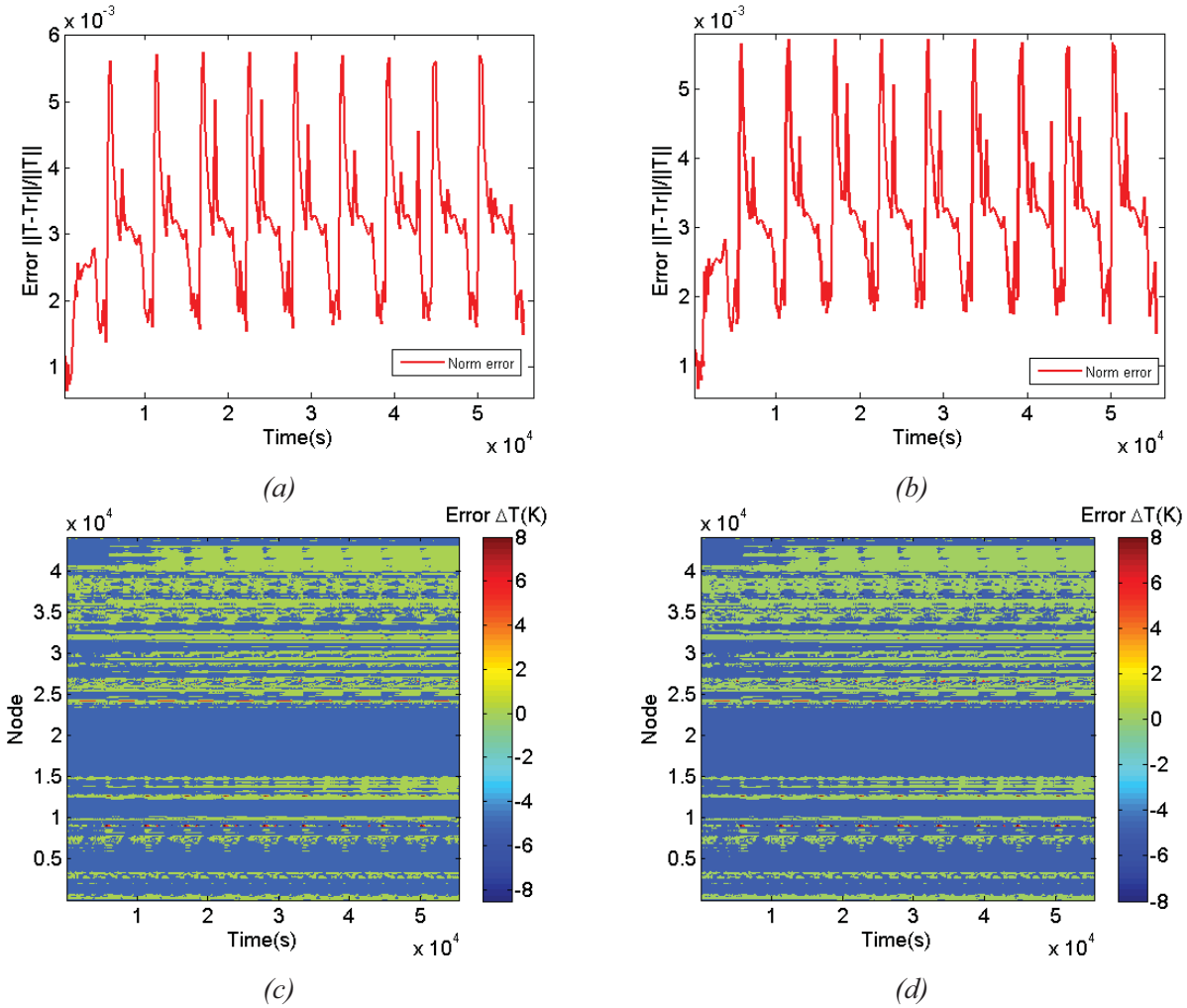

Figure 14. Simulation results of the TPWL-ROM (k=24) vs. the full-scale GPM model: (a, c) Relative error and absolute error, respectively, for ROM based on Constraint-1; and (b, d) Relative error and absolute error, respectively, for ROM based on Constraint-3.

4. CONCLUSIONS

In this paper, we presented a mathematically rigorous, subspace projection-based reduced order modeling (ROM) methodology for fast and efficient spacecraft thermal analysis. The detailed procedure of acquiring the whole spacecraft thermal model from the SINDA/FLUINT thermal analysis package and assembling it into an ODE/DAE form amenable for ROM was described. Two ROM methods, viz., proper orthogonal decomposition (POD) and trajectory piece-wise linear (TPWL), and their application to spacecraft thermal analysis for automated ROM generation were elucidated. In POD, the projection subspace is extracted from the solution snapshots using singular value decomposition (SVD) (or equivalent eigenvalue decomposition [35]), and the ROM is obtained by directly projecting the full-scale model onto the projection subspace. On the other hand, the TPWL-ROM is generated by weighted combination/interpolation of the localized linear ROMs to mimic the overall nonlinear dynamic behavior of the spacecraft.

The computational performance of ROMs was demonstrated via case studies using NASA-relevant spacecraft thermal models, including the LISA and GPM. Depending on the nature of various thermal

models, different usage scenarios of the ROM were proposed. For the model with a small number of independent heat sources, e.g., LISA, carefully designed input function can be employed in the training simulation to reveal their individual contribution to the dynamic response of the system, and hence, the model generation in this case is a one-time cost and the generated ROM can be reused for various operating scenarios. For example, the LISA ROM can be used in various simulations involving different heat flux values (within the limit prescribed during the training simulation) and oscillating frequencies (0.1 and 1 mHz). The reusability of ROM enables several orders of magnitude acceleration in computational speed and significant resource usage relative to the full-scale model without appreciable compromise in simulation accuracy. For the model with a large number of independent heat sources, e.g., the GPM model, training simulation scanning through each individual source contribution becomes a formidable challenge. Therefore, spacecraft orbit analysis is targeted as the primary ROM application in this scenario, in which a small number of orbits (typically 1-2) are simulated using the full-scale model, the harvested data are used for subspace and ROM generation, and the ROM is then utilized for the rest orbits, typically yielding 5× – 10× speedup including the initial full-scale simulation ROM generation (>100× if these costs are not considered). In both case studies (LISA and GPM), POD-ROM and TPWL-ROM were verified by comparing against the high-fidelity, full-scale model, which exhibited excellent agreement in spatiotemporal thermal profiles (<1% relative error).

The salient capability to capture spatiotemporal thermal behaviors that is otherwise unavailable by empirical models and the salient speedup over the full-blown analysis verified the utility of ROMs for initial concept screening, operational optimization, and thermal control and management. It should be noted that the present ROM is built on fixed operating and orbit parameters. To extend the current ROM framework to accommodate multi-parameter operations using sampling techniques for spacecraft design optimization [10, 11] will be the focus of our future work, which will effectively mitigate the aforementioned model reusability issues and significantly enhance the utility of the ROM.

ACKNOWLEDGEMENTS
This research is sponsored by NASA under contract number NNX11CB02C.

REFERENCES

1. Gilmore, D. and R. Collins, *Thermal design analysis.* Satellite Thermal Control Handbook, 1994: p. 5.
2. Karam, R.D., *Satellite Thermal Control for Systems Engineers*. 1998: American Institute of Aeronautics & Astronautics.
3. Kang, C., et al. *Satellite Thermal Modeling Techniques and Computation Tools*. in *The 40th Conference on Aeronautics and Astronautics, ROC*. 1998.
4. Moffitt, B.A. and J. Batty. *Predictive Thermal Analysis of the Combat Sentinel Satellite, 16 th AIAA*. in *USU Conference on Small Satellites-www. prism. gatech. edu (em inglês)*. 2002.
5. Uygur, A.B., et al. *Development of an in-house computer code for the thermal analysis of satellites using thermal network method and method of lines*. in *Recent Advances in Space Technologies, 2009. RAST'09. 4th International Conference on*. 2009. IEEE.
6. Tsai, J.-R., *Overview of satellite thermal analytical model.* Journal of spacecraft and rockets, 2004. **41**(1): p. 120-125.
7. Alvarez-Hernandez, A. and S.W. Miller, *Orion Project: Alternate Attitude Study.* 2009.
8. Gogu, C., et al., *Dimensionality reduction approach for response surface approximations: application to thermal design.* AIAA journal, 2009. **47**(7): p. 1700-1708.
9. Prince, J.L., J.A. Dec, and R.H. Tolson, *Autonomous aerobraking using thermal response surface analysis.* Journal of Spacecraft and Rockets, 2009. **46**(2): p. 292-298.

10. Miller, S.W. and E.J. Meier. *Development of a response surface thermal model for orion mated to the international space station*. in *Thermal and Fluids Analysis Workshop NASA*. 2010.
11. Miller, S.W. and W.Q. Walker, *Improvements to a Response Surface Thermal Model for Orion.* 2011.
12. Aling, H., et al. *Nonlinear Model Reduction with Application to Rapid Thermal Processing*. in *35th Conference on Decision and Control*. 1996. Kobe, Japan.
13. Białecki, R., A. Kassab, and A. Fic, *Proper orthogonal decomposition and modal analysis for acceleration of transient FEM thermal analysis.* International journal for numerical methods in engineering, 2005. **62**(6): p. 774-797.
14. Efe, M.O. and H. Ozbay. *Proper orthogonal decomposition for reduced order modeling: 2D heat flow*. in *Control Applications, 2003. CCA 2003. Proceedings of 2003 IEEE Conference on*. 2003. IEEE.
15. Banerjee, S., J.V. Cole, and K.F. Jensen, *Nonlinear model reduction strategies for rapid thermal processing systems.* Semiconductor Manufacturing, IEEE Transactions on, 1998. **11**(2): p. 266-275.
16. Bond, B.N. and L. Daniel, *A piecewise-linear moment-matching approach to parameterized model-order reduction for highly nonlinear systems.* IEEE Transactions on Computer-Aided Design of Integrated Circuits and Systems, 2007. **26**(12): p. 2116-2129.
17. Yang, Y.J. and K.Y. Shen, *Nonlinear heat-transfer macromodeling for MEMS thermal devices.* Journal of Micromechanics and Microengineering, 2005. **15**(2): p. 408-418.
18. Tiwary, S.K. and R.A. Rutenbar. *Faster, parametric trajectory-based macromodels via localized linear reductions*. in *Proceedings of the 2006 IEEE/ACM international conference on Computer-aided design*. 2006. ACM.
19. Voß, T. *Model reduction for nonlinear differential-algebraic equations*. in *Communications to SIMAI Congress*. 2007.
20. Manhart, M. and H. Wengle, *A spatiotemporal decomposition of a fully inhomogeneous turbulent flow field.* Theoretical and computational fluid dynamics, 1993. **5**(4-5): p. 223-242.
21. Wang, Y., et al., *Model Order Reduction*, in *Encyclopedia of microfluidics and nanofluidics*, D. Li, Editor. 2008, Springer: New York. p. 1382-1391.
22. Chaturantabut, S. and D.C. Sorensen, *Nonlinear model reduction via discrete empirical interpolation.* SIAM Journal on Scientific Computing, 2010. **32**(5): p. 2737-2764.
23. Chaturantabut, S. and D.C. Sorensen. *Discrete empirical interpolation for nonlinear model reduction*. in *Decision and Control, 2009 held jointly with the 2009 28th Chinese Control Conference. CDC/CCC 2009. Proceedings of the 48th IEEE Conference on*. 2009. IEEE.
24. Hochman, A., B.N. Bond, and J.K. White. *A stabilized discrete empirical interpolation method for model reduction of electrical, thermal, and microelectromechanical systems*. in *Proceedings of the 48th Design Automation Conference*. 2011. ACM.
25. Chaturantabut, S. and D.C. Sorensen, *A state space error estimate for POD-DEIM nonlinear model reduction.* SIAM Journal on numerical analysis, 2012. **50**(1): p. 46-63.
26. Rewienski, M. and J. White, *A trajectory piecewise-linear approach to model order reduction and fast simulation of nonlinear circuits and micromachined devices.* Computer-Aided Design of Integrated Circuits and Systems, IEEE Transactions on, 2003. **22**(2): p. 155-170.
27. Rewieński, M. and J. White, *Model order reduction for nonlinear dynamical systems based on trajectory piecewise-linear approximations.* Linear algebra and its applications, 2006. **415**(2): p. 426-454.
28. Vasilyev, D., M. Rewienski, and J. White, *Macromodel generation for bioMEMS components using a stabilized balanced truncation plus trajectory piecewise-linear approach.* IEEE Transactions on Computer-Aided Design of Integrated Circuits and Systems, 2006. **25**(2): p. 285-293.

29. Odabasioglu, A., M. Celik, and L.T. Pileggi. *PRIMA: passive reduced-order interconnect macromodeling algorithm*. in *Proceedings of the 1997 IEEE/ACM international conference on Computer-aided design*. 1997. IEEE Computer Society.
30. *SINDA/FLUINT*. Available from: http://www.crtech.com.
31. Merkowitz, S.M., et al. *Structural, thermal, optical and gravitational modelling for LISA*. 2004. Iop Publishing Ltd.
32. Peabody, H. and S. Merkowitz. *LISA thermal design*. 2005. Iop Publishing Ltd.
33. Krishnaprasad, P. and A.J. Newman, *Nonlinear Model Reduction for RTCVD*. 1998, MARYLAND UNIV COLLEGE PARK INST FOR SYSTEMS RESEARCH.
34. Sirisup, S., et al., *Equation-free/Galerkin-free POD-assisted computation of incompressible flows.* Journal of Computational Physics, 2005. **207**(2): p. 568-587.
35. Wikipedia, S. and B. Llc, *Singular Value Decomposition: Eigenvalue, Eigenvector and Eigenspace*. 2010: General Books LLC.

Appendix:

This appendix describes the process of assembling the node-wise information into **A**, **R**, $\mathbf{A}_s$, and $\mathbf{R}_s$ matrices for thermal modeling of the whole spacecraft. $\mathbf{A}\in\Re^{n\times n}$ and $\mathbf{R}\in\Re^{n\times n}$ is filled with the values of the conductive and radiative conductors in the model as illustrated in Eq. (A1). K_{ij}, R_{ij}, are, respectively, the conductive and radiative links between the i^{th} node and its 'thermally' adjacent nodes (via conduction or radiation). K_{si} and R_{si} are the conductive and radiative link between the i^{th} node and an isothermal object (e.g., space), respectively. The value of K_{si} and R_{si} would be zero if the node has no flux exchange with the isothermal object. Therefore, $\mathbf{A}_s$ and $\mathbf{R}_s$ are diagonal matrices storing K_{si} and R_{si} for each node as Eq. (A2).

$$\mathbf{A}=\begin{bmatrix} -\left(\sum_j^{N_i} K_{ij}\right)-K_{si} & & K_{ij} \\ & \cdots & \\ K_{ij} & & -\left(\sum_k^{N_j} K_{jk}\right)-K_{sj} \end{bmatrix},\ \mathbf{R}=\begin{bmatrix} -\left(\sum_j^{M_i} R_{ij}\right)-R_{si} & & R_{ij} \\ & \cdots & \\ R_{ij} & & -\left(\sum_k^{M_j} R_{jk}\right)-R_{sj} \end{bmatrix} \quad \text{(A1)}$$

$$\mathbf{A}_s=\begin{bmatrix} \ddots & & 0 \\ & K_{si} & \\ 0 & & \ddots \end{bmatrix},\ \mathbf{R}_s=\begin{bmatrix} \ddots & & 0 \\ & R_{si} & \\ 0 & & \ddots \end{bmatrix}. \quad \text{(A2)}$$

Subject to energy conservation, the entries in the i^{th} row of matrix **A** and **R** need to satisfy

$$\sum_j^n A_{ij}=-K_{si} \quad \text{and} \quad \sum_j^n R_{ij}=-R_{si} \quad \text{(A3)}$$

This signifies that energy input to the i^{th} node equals to that drawn from its 'thermally' adjacent nodes.